Molecular insight into nano-heterogeneity of localized high-concentration electrolyte: Correlation with lithium dynamics and solid-electrolyte interphase formation

Long Su [b], Fei Lu [a], Xu Liu [c,d], Chunting Wang [b], Yanan Gao [a], Stefano Passerini [c,d], Liqiang Zheng [b], Gao Xinpei [a,*]

[a] *Key Laboratory of Ministry of Education for Advanced Materials in Tropical Island Resources, Hainan University, No 58, Renmin Avenue, Haikou, 570228, China*
[b] *Key Laboratory of Colloid and Interface Chemistry, Shandong University, Ministry of Education, Jinan, 250100, PR China*
[c] *Helmholtz Institute Ulm (HIU), Helmholtzstrasse 11, 89081, Ulm, Germany*
[d] *Karlsruhe Institute of Technology (KIT), P.O. Box 3640, 76021, Karlsruhe, Germany*

GRAPHICAL ABSTRACT

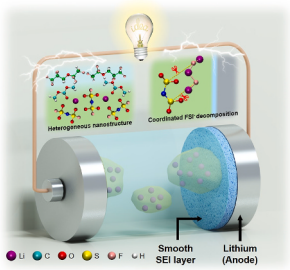

ARTICLE INFO

Dedicated to Professor Emanuel Peled on the occasion of his 80th birthday

Keywords:
Localized high-concentration electrolytes
Solvation structure
Solid electrolyte interphase
Lithium metal battery

ABSTRACT

Localized high-concentration electrolytes (LHCEs) have attracted extensive attention in light of their excellent characteristic that inherits the advantages of high-concentration counterparts and minimize their shortcomings. However, the fundamental mechanisms of nano-heterogeneity influencing the LHCE properties are still not well understood. Herein, a systematic comparison combining theoretical and experimental methods is performed to clarify the fundamental correlation between electrolyte microstructure and properties. The unique microstructure in the LHCE of high-concentration clusters surrounded by a nonsolvating diluent enables the hopping diffusion of Li^+ through the anion ligand layers, which is responsible for the high transference number and fast diffusion of Li^+. In addition, the anion coordinated with multiple Li^+ undergoes defluorination reactions and contributes, with the diluent decomposition, to the formation of a stable and robust "LiF-rich" solid electrolyte interphase (SEI) layer on the Li metal, which is responsible for the enhanced cycling stability. These fundamental insights highlight the correlation of microstructural and dynamic heterogeneities of electrolytes with SEI formation, which should be considered in the rational design of next-generation improved electrolytes.

* Corresponding author.
E-mail address: xpgao@hainanu.edu.cn (G. Xinpei).

1. Introduction

The thriving market of electric vehicles, portable electronics, and smart grid energy storage has stimulated extensive efforts to design batteries with high energy densities and intrinsic safety. Owing to the superhigh specific capacity (3862 mAh g ^{1}) and low standard reduction potential (3.040 V vs. the standard hydrogen electrode [SHE]) of Li metal, Li-metal batteries (LMBs) are regarded as the "holy grail" of next-generation high energy-density battery systems [1–3]. The development of LMBs is largely hindered by two critical barriers, its low Coulombic efficiency (CE) and the dendrite growth over cycling [4–6]. Highly dendritic Li deposition morphologies severely reduce Li utilization and cycle life and induce serious safety concerns due to the internal short circuit [7–9]. To suppress dendrite formation in the practical application of LMBs, significant efforts have been devoted to enhancing the stability and uniformity of the solid electrolyte interphase (SEI) layer formed at the Li/electrolyte interface [10]. Hence, a suitable electrolyte is vital to improve battery performance, since electrolyte components are directly related to the formation/evolution of the SEI layer, which in turn influences the dynamics and deposition of Li ions [11–13].

Generally, an ideal electrolyte should be able to regulate Li^+ transport and suppress Li dendrite growth at the electrode/electrolyte interface [14–16]. To fulfill this requirement, tremendous efforts have been devoted to achieve compact and uniform Li deposition by novel solvent design [17], protective coatings [18], and addition of functional additives [19]. Among these multiple approaches, increasing salt concentration to form high-concentration electrolyte (HCE) has received increasing attention benefitting from its enhanced Li plating/stripping performance as well as inhibited dendrite growth in LMBs [20–23]. Nevertheless, HCEs suffer several limitations in practical applications, such as high Li salt cost and high viscosity [24]. Recently, the localized high-concentration electrolytes (LHCEs) prepared by adding non-solvating diluents to HCEs have attracted extensive attention in light of the characteristic that inherits the advantages of HCEs and minimize their shortcomings [25–28]. With a change in the solvation structures from solvent-separated ion pairs (SSIPs) in low-concentration electrolytes (LCEs) to contact ion pairs (CIPs) or clusters in concentrated electrolytes, an extraordinary solvation structure of LHCE emerges upon the addition of a diluent. However, electrolyte microstructure evolution after the addition of a diluent and the localized high-concentration effect on ionic transport mechanism and SEI formation remain unclear.

The formation of HCEs is generally considered as the foundation of LHCE functionality [14,29]. Although experiments and calculations have provided insight into the electrolyte microstructures of LHCEs, previous studies mainly focused on the local solvation structure, i.e., salt anions and solvent molecules [30–32]. However, these studies are insufficient to explain the unique properties of LHCEs. The effect of nanostructures beyond well-studied local ion solvation structures, such as clusters and aggregates, on the ionic transport and SEI formation in LHCEs is not well understood. To reveal the fundamental understanding behind the difference in the performance of LCEs, HCEs, and LHCEs, the microstructural evolution, concentration changes, and diluent incorporation, which significantly affect ionic transport and SEI formation, have been systematically characterized by combining experimental and theoretical methods. Comparative studies were performed by revisiting conventional carbonate-based electrolytes comprising 1 M and 4 M lithium bis(fluorosulfonyl)imide (LiFSI) in dimethyl carbonate (DMC) as a basis LCE and HCE, respectively. In common wisdom, the electrolyte with carbonate solvent solvents suffer from severe side reactions with Li metal. A series of LHCEs were prepared by adding a commonly fluorinated ether, 1,1,2,2-tetrafluoroethyl-2,2,3,3-tetrafluoropropyl ether (TTE), as a cost effective cosolvent to yield the 1 M LiFSI electrolyte with a hybrid DMC/TTE solvate. Electrochemical cycling tests revealed that the LHCEs exhibited significantly enhanced plating/stripping cycling stability, compared with those of the HCE and LCE. Comprehensive structural analyses suggested that LHCEs exhibited a heterogeneous electrolyte nanostructure, which featured more Li^+ in clusters and were associated with bridging FSI anions with multiple coordinated sites. The solvent DMC was located at the cluster surface to coordinate with Li^+, acting as the boundary between the $Li^+(FSI)_x(DMC)_y$ cluster and TTE-rich domain. The heterogeneous nanostructure in the LHCE enabled Li^+ hopping diffusion and enhanced the Li^+ transference number. Importantly, it was evident from the simulation and experiment that the local Li^+ solvation structure of LHCE surrounded by dilute TTE contributed to the predominant FSI decomposition, which, along with the TTE decomposition, led to compact and smooth SEI layers. This was considered responsible for inhibiting Li dendritic growth and enhancing plating/stripping cycling stability. The identification and evaluation of the effect of electrolyte microstructure on battery performance are expected to trigger a new design of advanced electrolytes for next-generation LMBs.

2. Computational methods and experimental section

2.1. Electrolyte preparation

DMC (99.5%, Sigma Aldrich) and TTE (99%, Apollo Scientific) were dried with the activated molecular sieves (3 Å, Alfa Aesar), which were activated at 300 °C under vacuum (10 ^{3} mbar) for more than one week. LiFSI (99%, PROVISCO CS) was dried at 120 °C under vacuum (10 ^{3} mbar) for 24 h before use. PE separator (SV718, Asahi Kasei Company) was dried at 40 °C under vacuum (10 ^{3} mbar) for 24 h. Li metal foils (thickness 500 μm, 99.9%, Honjo Metal Co., LTD) were used as received. The electrolyte preparation and cell assembly were conducted in an Ar-filled glove box with H_2O and O_2 levels $\leq$0.1 ppm. The water content in the prepared electrolytes was determined to be lower than 15 ppm via a Karl-Fischer titrator (C30, METTLER TOLEDO) in a dry room with a dew point lower than 65 °C.

2.2. Physical and electrochemical measurements

The DDS-307A conductivity meter (Leici Co., Ltd.) was performed to measure the ionic conductivity of the electrolytes at 298 K. Viscosity measurements were carried out on a Haake RS300 Rheometer with a coaxial cylinder sensor system. The diffusion ordered spectroscopy (DOSY) nuclear magnetic resonance (NMR) experiments were performed on a Bruker Avance III HD 400 MHz NMR spectrometer with a 5 mm NMR tube at room temperature. The diffusion coefficients of Li^+ were calculated with Stejskal-Tanner equation: $S(g)/S(0) = \exp[-D\gamma^2g^2\delta^2(\Delta \quad \delta/3)]$, where S(g) is the intensity as a function of gradient, D is the diffusion coefficient, γ is the gyromagnetic ratios of ^{7}Li, g is the gradient strength, Δ is the gradient pulse interval, and δ is the duration pulse. Raman spectrometer (HORIBA LabRAM HR Evolution) were performed to characterize the microcosmic structure of electrolytes. X-ray photoelectron spectroscopy (XPS) tests were conducted using Thermo Fisher K-Alpha + spectrometer using monochromic Al Kα radiation. All the samples were recovered from the Li||Cu cell after 10th electrochemical cycling. The samples were washed with DMC and then dried under vacuum before XPS tests.

Electrochemical cycling was performed using CR2032-type coin cells. Li discs with a diameter of 14 mm were used as the electrodes, and 50 μL electrolyte was added into each cell. The electrochemical tests were conducted at 20 °C with a galvanostat/potentiostat VMP (Bio-Logic, France). The detailed morphologies of the Li anode in the cycled

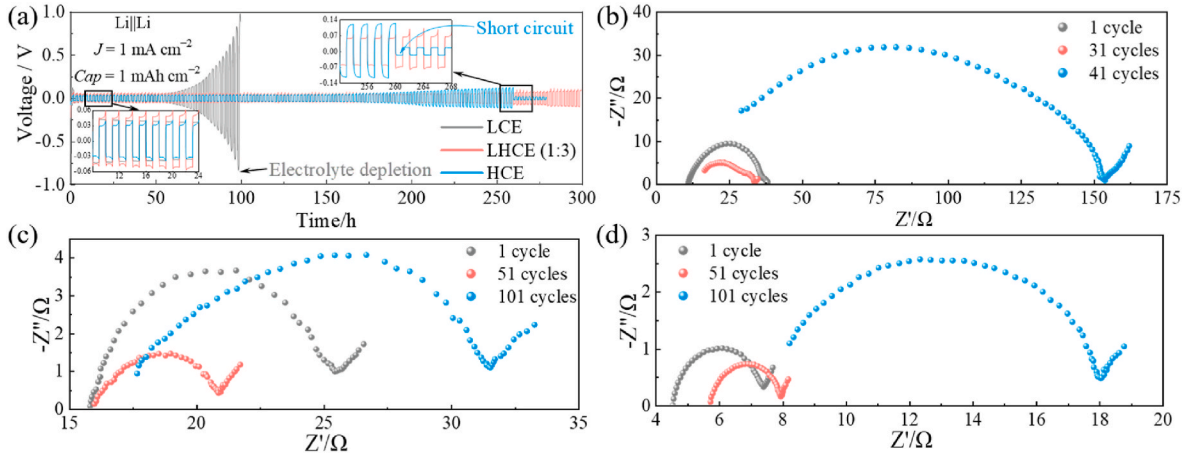

Fig. 1. (a) Cycling performance of Li||Li symmetric cells using various electrolytes at a current density of 1 mA cm^{-2} and cycling capacity of 1 mAh cm^{-2}. Nyquist plots of Li||Li symmetric cells with (b) LCE, (c) LHCE, and (d) HCE after different cycles.

Li||Li cells in various electrolytes after 50th cycles were explored by scanning electron microscopy, which were obtained from a Zeiss CrossBeam XB340 microscope equipped with an energy dispersive X-ray detector.

2.3. Computational methods

Classical molecular dynamics simulations: Classical molecular dynamics (CMD) simulations were conducted for LCE, LHCE, and HCE systems using the GROMACS 2020.6 [33] software to investigate the dynamics properties and solvation structure. The molecular structure and the details of the simulated systems were presented in Fig. S1 and Table S1 in the Supporting Information. Simulation details keep consistency with previous publication [34,35]. The force-fields parameters of Li^+, FSI , DMC, and TTE are taken from Refs. [36–38]. Initial configurations with periodic boundary conditions in XYZ directions were constructed using Packmol code [39]. An energy minimization was performed to minimize the energy of the initial configuration using steepest descent method [40] employing a convergence criterion of 500 kJ mol ^{1} nm ^{1}. NPT ensemble was performed for 30 ns to obtain the correct density of the electrolytes using the V-rescale thermostat method [41]. The V-rescale temperature coupling method [42] was applied to couple the temperature. All systems were melted to 340 K with an equilibration simulation and then subsequently annealed from 340 K to 298 K. Afterward, a 10 ns production simulation was performed in NVT ensemble for subsequent analysis. Furthermore, the particle mesh Ewald (PME) method [43] and Lennard-Jones potential were utilized to describe long-range electrostatic interactions and van der Waals interaction with a cutoff of 1.2 nm. The LINCS algorithm [44] was used to constrain the bond length to the equilibrium values. The force field parameters were benchmarked against the experimental density and found to reproduce the experimental values adequately, the details of which are provided in Table S2 in the Supporting Information. All the simulations were conducted for at least three times to ensure reproducibility.

Ab initio molecular dynamics simulations: Based on the analysis of CMD simulation and experiments, representative LCE, LHCE, and HCE systems were constructed for Ab initio molecular dynamics (AIMD) simulations using the Quickstep module [45] of the CP2K package with Gaussian plane wave (GPW) method. The composition of the simulated systems was listed in Table S3 in the Supporting Information. The double-ζ valence basis sets with a polarization function for all atoms were used. The Perdew-Burke-Ernzerhof (PBE) generalized-gradient exchange-correlation functional [46] was adopted to reproduce the structural properties of electrolytes. All AIMD simulations were performed in the NVT ensemble under periodic boundary conditions. The cutoff is set to 1000 Ry. The projected density of state (PDOS) for FSI , DMC, and TTE was calculated by utilizing a powerful software named Multiwfn [47] based on the equilibrium configuration of AIMD simulations. In addition, electrons were inserted into the simulation cell sequentially every 2 ps to investigate the electrolyte solvation effect on SEI layer formation with an excess of electrons.

3. Results and discussion

First, a representative example of LHCE (1:3) was developed in this study. It was constructed using 1 M LiFSI dissolved in a hybrid solvent, DMC/TTE, at a volume ratio of 1:3. An LCE (1 M FSI/DMC) and HCE (4 M FSI/DMC) without TTE were explored for comparison. Fig. 1a shows the cycling stability of Li||Li symmetric cells for three electrolytes at a current density of 1 mA cm ^{2} and cycling capacity of 1 mAh cm ^{2} for each plating/stripping process. As shown in Fig. 1a, after the initial cycles, the cells demonstrated a similar and stable voltage response of Li plating/stripping. However, the LCE enabled stable cycling for less than 60 h with the Li||Li cell because of electrolyte depletion, which correlated with that in a previous study [48], followed by a dramatic voltage polarization increase after several cycles, leading to cell failure. The dominant structures of SSIPs and continuous parasitic reactions of the coordinated DMC and the highly reactive Li metal during cycling are responsible for the poor interfacial stability of LCE against the Li metal. As expected, with an increase in the salt concentration, the Li||Li cell with HCE exhibited relatively stable cycling for approximately 260 h before the short circuiting occurred, which was highly related to Li dendrites. Contrarily, a further enhanced cycle stability (>300 h) was obtained with the dilution of TTE in the Li||Li cell with LHCE (1:3), along with a stable low electrode polarization (<0.2 V) during cycling. The improved cycling stability revealed that the introduced diluent (TTE) effectively prevented the parasitic reactions of DMC with Li metal and enhanced the interfacial stability between the Li metal and electrolyte.

Furthermore, the interfacial reaction kinetics of Li||Li symmetrical cells with different electrolytes were monitored by electrochemical impedance spectroscopy during cycling. As shown in Fig. 1b–d, the high-frequency intercept was designated as the ohmic resistance (R_s), whereas the second intercept in the low-frequency region shows the interfacial (R_i) resistance, which combined the resistance of the migration of Li^+ through the SEI layer (R_{SEI}) and charge-transfer resistance (R_{ct}). The R_s values fitted via the equivalent circuit were approximately

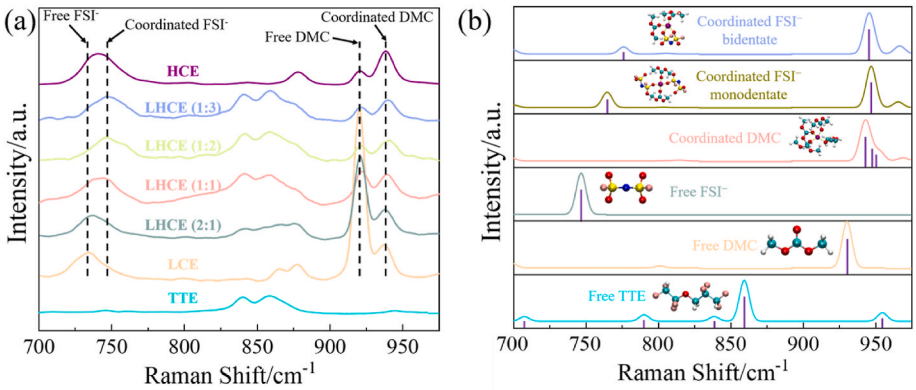

Fig. 2. (a) Progression of Raman spectra of different electrolytes and neat TTE during the experiment. (b) Theoretical Raman spectra of free and coordinated molecules. Theoretical Raman spectra were recorded at the optimized geometries at the B3LYP/6–311++G** level, and the optimized geometries are shown as the inset.

11, 16, and 5 Ω for LCE, LHCE (1:3), and HCE, respectively, prior to cycling. After 101 cycles, the R_s values for LHCE (1:3) and HCE slightly increased to 17 and 8 Ω, respectively. Contrarily, the R_s value for LCE decreased to 9 Ω after 41 cycles, which was attributed to the continuous consumption of Li salt during cycling [49]. Changes in R_i are usually directly related to the reconstruction of the SEI layer caused by the Li stripping/plating cycles [50]. Noteworthily, the R_i of the cell with LCE significantly increased from 26 to 145 Ω after 41 cycles, indicating that the parasitic reactions between Li metal and electrolytes led to the continuous depletion of electrolytes [30]. Regarding the impedance, the lower R_i value indicated that the SEI layer formed in LHCE (1:3) was more stable and conductive on the Li metal, which was favorable for enhancing Li^+ ion transport [51]. These observations are in good agreement with the enhanced interfacial stability between the LHCE (1:3) and Li metal.

The cycling capacity of Li||Li symmetric cells is directly related to the local solvation structures and microstructures of electrolytes, which determines the ionic transport mechanism and SEI composition. Therefore, a series of LHCEs were constructed using 1 M LiFSI dissolved in a hybrid solvent (DMC/TTE) (volume ratios = 2:1, 1:1, 1:2, and 1:3), and the effect of TTE addition on the electrolyte solvation structure was systematically investigated using experimental and theoretical methods. The progression of Raman spectrum for different electrolytes and neat TTE was performed to determine the local Li^+ solvation structure formed in these electrolytes (Fig. 2a), while the complete Raman spectrum was shown in Fig. S2 in the Supporting Information. Theoretical Raman spectrum calculations of the free molecules and ion pairs at the optimized geometries were performed as references to assign the Raman bands (Fig. 2b) [38]. As expected, compared with the spectrum of the neat TTE solvent, no Raman shifts were observed after introducing the TTE in LHCEs (Fig. 2a), suggesting that TTE had a minimal effect on the local Li^+ solvation structure [52,53]. Moreover, based on theoretical results, the intense peak exhibited a blueshift when free DMC was coordinated with Li^+. Correspondingly, the free and coordinated DMC peaks observed during the experiment were fitted using a Gaussian function (Fig. S3). It was observed that the peak intensity of free DMC at ~921 cm^{-1} gradually decreased, while the coordinated DMC at ~939 cm^{-1} grew with an increasing salt concentration or diluent content [54]. As shown in Fig. 2a, the intense peak at ~733 cm^{-1} assigned to free FSI confirmed that SSIPs were the dominant species in the LCE. The intense peak attributed to FSI was gradually blueshifted from ~733 to ~746 cm^{-1} with an increasing diluent (TTE) content. It is worth noting that the theoretical results also show that the enhanced interaction between FSI and Li^+ induced the peak blueshift. The HCE exhibited a similar Raman expansion–contraction mode in the DMC region, similar to that of the LHCE (1:3). However, there was a clear misalignment of the broad vibration peak of FSI in the HCE and LHCE (1:3) (~746 cm^{-1} for LHCE (1:3), ~740 cm^{-1} for HCE), which could be attributed to more FSI in HCE being coordinated to Li through monodentate geometries, compared with LHCE (1:3) (Fig. S4). This was supported by the theoretical results that the intense peak of FSI in bidentate geometry exhibited slight blueshifts, compared with monodentate geometry.

Based on the Raman spectroscopy analysis of the local Li^+ solvation structures in LCE, LHCE, and HCE, classical molecular dynamics (CMD) simulations were performed to explore electrolyte microstructures at a large scale. Through the characterization of radial distribution functions (RDFs) and coordination number of different species around Li^+ (Fig. 3a and S5), the high solvent/salt ratio showed that Li^+ was accompanied by four DMC molecules in LCE, while the FSI were mostly excluded from the Li^+ solvation structures, indicating the formation of dominant SSIPs [55]. Fig. 3b shows the ion agglomeration number and percentage of Li^+ located in different sizes of ion agglomeration in the electrolytes. The total Li^+ in LCE was distributed in an ion agglomeration containing only one Li^+, confirming that the SSIPs were the dominant species in LCE. Representative simulation snapshots of LCE (Fig. 3d) also confirmed that the Li^+ were uniformly distributed throughout the DMC solvent in the LCE, while FSI were free from the Li^+ solvation structures. When the salt concentration increased to 4 M (HCE), nearly all the DMC molecules were coordinated with Li^+ (Fig. S6a). Therefore, since the DMC molecules could not completely solvate the Li^+ species, the entry of FSI into the Li^+ solvation layers were inevitable, forming a variety of local Li^+ solvation layers comprising FSI and DMC.

Subsequently, compared with LCE, the number of coordinated DMC in the Li^+ solvation structures reduced, and the number of coordinated FSI was enhanced with the increasing diluent TTE content in LHCEs (Fig. 3a). The TTE molecules were observed to be barely coordinated with Li^+ in the LHCEs, suggesting that the TTE molecules were outside the Li^+ first coordination shell, independent of the diluent content. Interestingly, the local Li^+ solvation structure of LHCE (1:3) was more similar to that of the HCE and different from that of the LCE at the same salt concentration. In addition, most of the Li^+ was located in large ion agglomerations containing more than two Li^+, indicating the formation of nanoscale clusters in the LHCE (1:3) and HCE (Fig. S6b). However, the simulation snapshots of LHCE (1:3) and HCE (Fig. 3e and f, respectively) exhibit significantly distinct electrolyte microstructures. Different from the homogeneous nanostructure in HCE, LHCE (1:3) exhibited a heterogeneous electrolyte nanostructure, which featured more Li^+ in clusters associated with bridging FSI anions with multiple coordinated sites, while the DMC molecules were located at the cluster surface. The diluent molecules always surrounded these $Li^+(FSI)_x(DMC)_y$ clusters. The RDF profiles of Li^+–Li^+ in the electrolytes confirmed the evolution of the electrolyte microstructure (Fig. 3c). A broad peak of Li^+–Li^+ was identified at ~0.92 nm for LCE, LHCE (2:1), and LHCE (1:1), reflecting the presence of SSIPs and CIPs. With a high salt concentration or

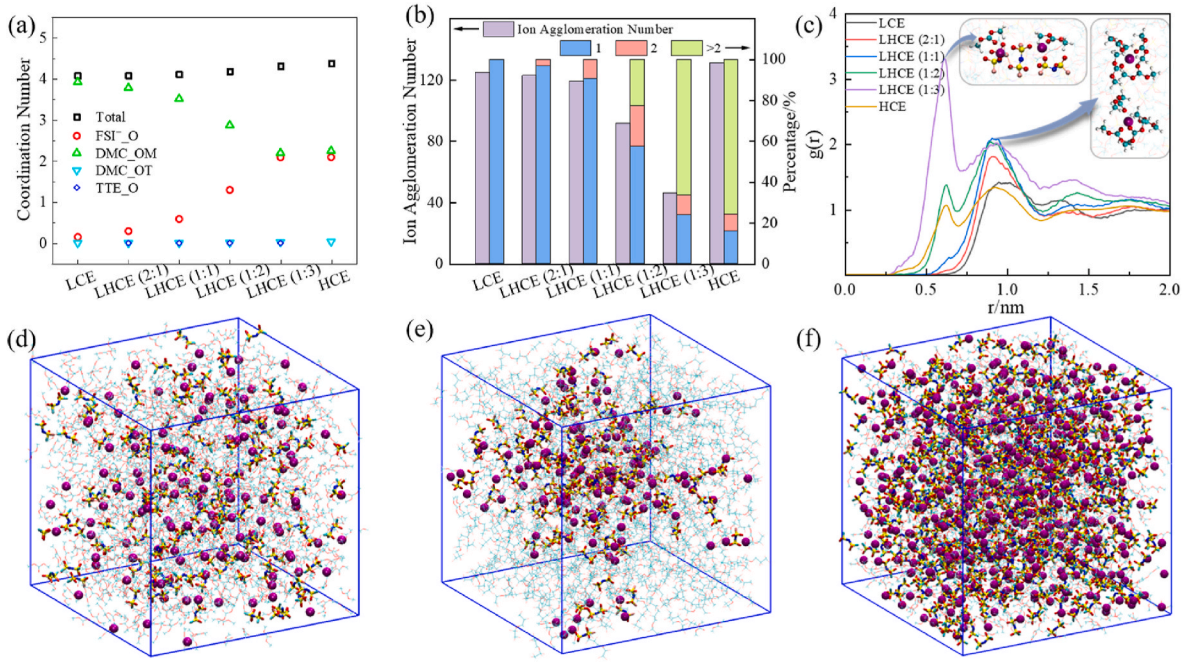

Fig. 3. (a) Average coordination number of each component around Li^+ in the electrolytes. (b) Ion agglomeration number and percentage of Li^+ in different sizes of ion agglomeration in the electrolytes. (c) RDF profiles of Li^+–Li^+ in electrolytes. Representative simulation snapshots of (d) LCE, (e) LHCE (1:3), and (f) HCE. Color code is similar to that in Fig. S1. (For interpretation of the references to colour in this figure legend, the reader is referred to the Web version of this article.)

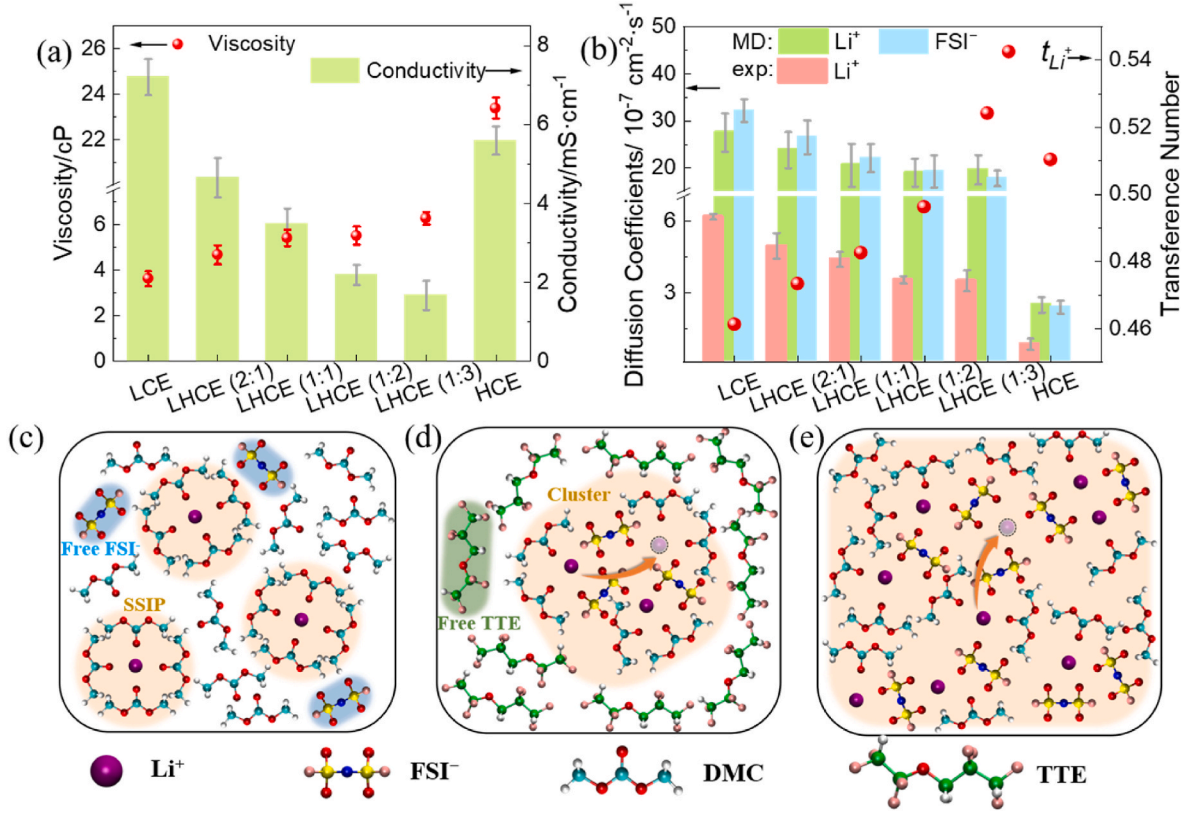

Fig. 4. (a) Viscosity and ionic conductivity of the LCE, LHCEs, and HCE. (b) Diffusion coefficients (D_{Li+}, D_{FSI-}) and transference number of Li^+ (t_{Li+}) in electrolytes obtained from MD simulation and DOSY-NMR. Schematic illustrations of the solvation structure and transport mechanism of (c) LCE, (d) LHCE, and (e) HCE.

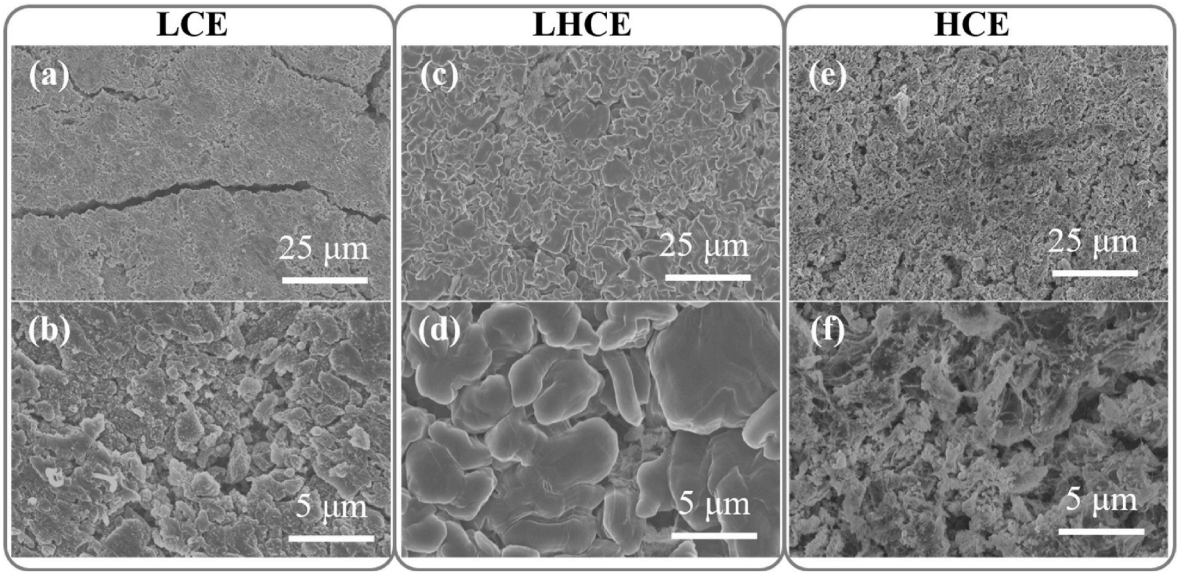

Fig. 5. SEM images of Li metal anodes in Li||Li symmetric cells for (a, b) LCE, (c, d) LHCE (1:3), and (e, f) HCE after 50 cycles at a current density of 1 mA cm^{-2} and cycling capacity of 1 mAh cm^{-2}.

sufficient diluent content, an additional sharp peak at ~0.61 nm, corresponding to the neighboring Li^+ share communal first coordination shell, was observed for LHCE (1:2), LHCE (1:3), and HCE, indicating the presence of nanoscale clusters or aggregates. The aforementioned experimental and theoretical analysis showed that the SSIPs were the dominant species in the LCE because of the strong coordinated interaction between DMC and Li^+. The increase in salt concentration or the addition of TTE induced a similar local Li^+ solvation structure in LHCE and HCE, comprising salt anions and solvent molecules. However, apart from the homogeneous aggregates in HCE, LHCE (1:3) tended to generate a heterogeneous electrolyte nanostructure, which featured $Li(FSI)_x(DMC)_y$ clusters surrounded by TTE.

The effects of the salt concentration and diluent content on the physical properties of electrolytes, such as viscosity and ionic conductivity, were investigated at 298 K. As shown in Fig. 4a, the significantly enhanced electrostatic interactions in the HCE dramatically increased the viscosity to 23.4 cP [approximately 6 times that of the LCE (3.5 cP)]. The excessive viscosity contributed to the poor wettability of the HCE toward the separator and electrode materials, which was unfavorable for its practical application [56]. Despite the high salt concentration in the HCE, the high viscosity restricted Li^+ motion, compared with that of the LCE (Fig. 4a). As expected, the dilution of TTE minimized the limitations of HCE. The viscosities of LHCE (2:1), LHCE (1:1), LHCE (1:2), and LHCE (1:3) were only 4.7, 5.4, 5.5, and 6.1 cP, which were significantly lower than that of HCE. We considered that the weak interaction between the two well-defined domains, the $Li(FSI)_x(DMC)_y$ cluster and TTE-rich domain reduced the viscosities of LHCEs, whereas virtually all solvents and FSI were highly associated and coordinated with the Li^+ in HCE (Fig. S6). Furthermore, the viscosity and ionic conductivity of LHCEs were negatively correlated. The ionic conductivities of LHCEs slightly decreased from 4.66 to 1.67 mS cm^{-1} with an increase in the TTE content. Compared with HCE, the improved physical properties of the LHCE and the reduced cost were highly favorable for practical applications.

Concerning transport mechanisms, the diffusion coefficients of Li^+ and FSI (D_{Li+}, D_{FSI}) stem from the slopes of the corresponding mean squared displacement curves are shown in Fig. 4b. Although the diffusion of Li^+ and FSI was restricted with increasing salt concentrations or the addition of TTE, the difference in the electrolyte microstructure induced a significant change in the stable diffusion ratios, $D_{Li+}/(D_{Li+} + D_{FSI})$, i.e., the transference number of Li^+ (t_{Li+}). It was observed that the t_{Li+} monotonically increased with an increase in the TTE content, indicating that TTE enhanced the transference number of Li^+. The t_{Li+} of LHCE (1:3) reached 0.52, which was even higher than that of the HCE. The simulated D_{Li+} was calibrated by diffusion ordered spectroscopy (DOSY) nuclear magnetic resonance (NMR) experiment (Fig. 4b). The evolution of D_{Li+} obtained from the simulation was proportional to the DOSY-NMR results, while the difference in absolute values was within one order of magnitude.

Notably, the ion transport mechanism is highly associated with the microstructure of electrolytes. For the LCE, the dominant Li^+ species were fully solvated by DMC as SSIPs, while FSI were screened out from the coordination layer to be free (Fig. 4c). Therefore, we considered that the dominant ionic diffusion mechanism in the LCE was vehicular transport, with Li^+ and its tightly bound DMC molecules diffusing as a single entity, which explained the lower t_{Li+} of LCE. After adding TTE to afford LHCE, the free DMC molecules and FSI disappeared to form clusters in a sea of TTE (Fig. 4d). The FSI in the clusters were mainly coordinated with multiple Li^+, while the DMC molecules were located at the cluster surface to coordinate with Li^+ acting as the boundary between the $Li^+(FSI)_x(DMC)_y$ cluster and TTE-rich domain. Although the vehicular diffusion of clusters and hopping diffusion through coordinated layers in the clusters coexisted in the LHCE and contributed to Li^+ diffusion, given the fact that the clusters were relatively immobile because of the large size, the hopping diffusion mechanism mainly contributed to Li^+ diffusion [34]. With an increase in the salt concentration, Li^+ were uniformly distributed in the HCE and formed continuous homogeneous aggregates, whereas virtually all the DMC molecules and FSI were drawn into the Li^+ solvation sheath (Fig. 4e). Although the vehicular diffusions of Li^+ and FSI were significantly restricted within the clusters, Li^+ diffused through exchange coordinated FSI in clusters via the hopping diffusion, which was responsible for the higher t_{Li+} of LHCE and HCE [57].

To analyze the microstructural and dynamic heterogeneities of electrolytes with SEI formation, the detailed morphologies of Li deposits of Li||Li symmetric cells in various electrolytes after 50 cycles were observed by scanning electron microscopy (SEM) (Fig. 5). The Li metal anode using LCE (Fig. 5a and b) exhibited an irregular growth with large cracks, indicating the continuous side reactions between the electrolyte and Li metal. Although the same conditions were used for the cycling tests, the cell with the LHCE (1:3) (Fig. 5c and d) exhibited a compact and smooth surface without cracks, indicating the formation of a robust

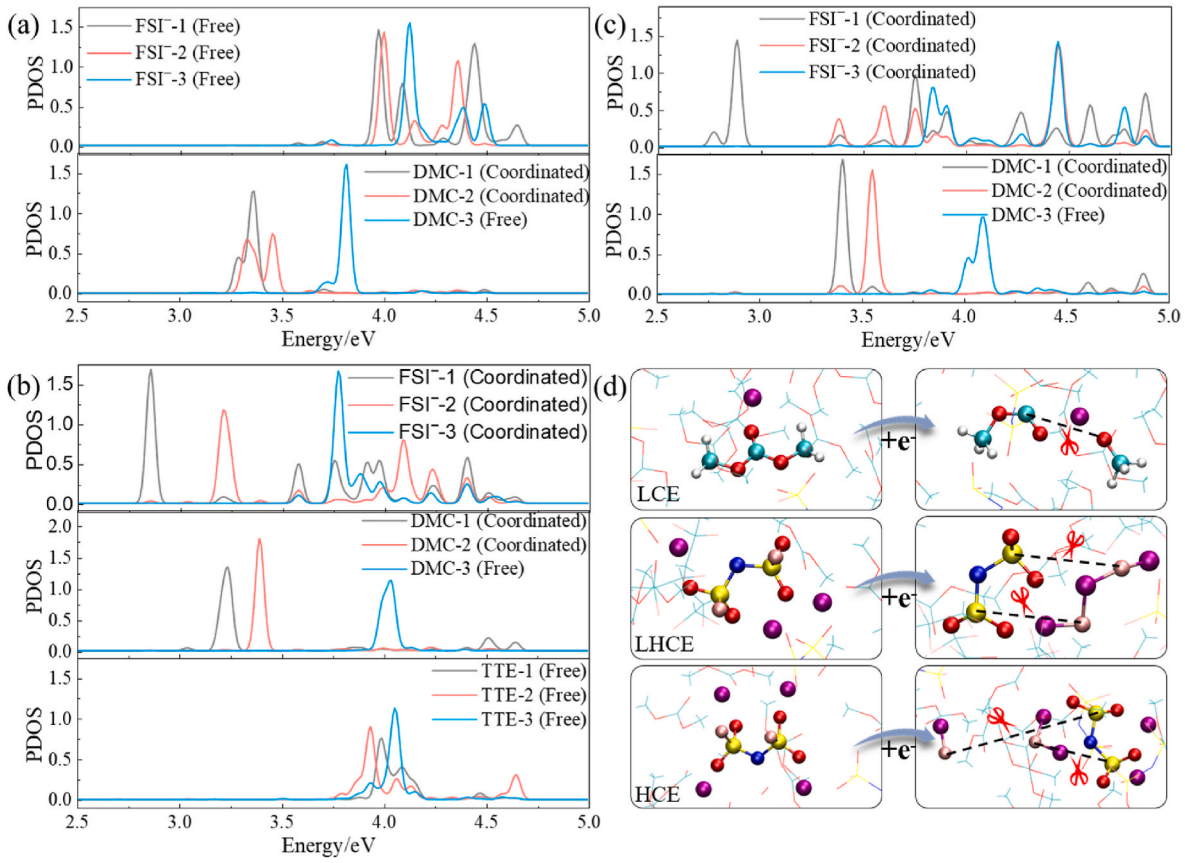

Fig. 6. Projected density of states (PDOS) of FSI^-, DMC, and TTE in the (a) LCE, (b) LHCE, and (c) HCE. (d) Reaction process observed in the AIMD simulations of LCE (top), LHCE (middle), and HCE (down) with the addition of electrons.

and dense SEI layer, which explained the enhanced cycling stability against the Li metal. Energy dispersive X-ray spectroscopy of deposited Li metal revealed that the SEI layers were rich in fluorine (Fig. S7), indicating the formation of a robust "LiF-rich" SEI layer. Therefore, the "LiF-rich" SEI layer was highly beneficial for suppressing side reactions between the Li metal and electrolytes. The Li metal anode in the cell using HCE exhibited relatively rough and porous structures (Fig. 5e and f), indicating inevitable Li dendrite formation, and finally, inducing the internal short circuit.

Based on the CMD simulation and experiments, representative LCE, LHCE, and HCE systems were constructed for *ab initio* molecular dynamics (AIMD) simulations to explore the mechanism of the suppressed side reactions and the enhanced cycling stability of the LHCE. Fig. 6a–c shows the projected density of states (PDOS) of the coordinated and free FSI , DMC, and TTE in the three electrolytes. The lowest unoccupied molecular orbital (LUMO) levels directly correlated with the reduction stability. The lower the LUMO level, the more preferentially the molecules were reduced. According to the analysis of the aforementioned solvation structure, part of the DMC molecules were coordinated with only one Li^+, while practically all the FSI were excluded from the coordination layer in the LCE. As demonstrated in Fig. 6a, the LUMO level was located at the coordinated DMC (DMC-1 and DMC-2), not the free DMC (DMC-3), indicating that the coordinated DMC was first reduced and exhibited a DMC-derived composition in the SEI formed in the LCE. With the evolution of the solvation structures from the SSIPs in the LCE to the clusters in the LHCE, the FSI -1 was coordinated with three Li^+ and exhibited lower LUMO levels than those of the coordinated DMC (Fig. 6b). This shifting toward a lower LUMO level induced the preferred decomposition of the coordinated FSI and inhibited the DMC decomposition on the Li-metal surface. In addition, it was highly beneficial for the formation of a stable SEI layer. Similar local solvation structures in LHCE and HCE led to similar interfacial reactions. An increase in the coordinated number of Li^+ to that of FSI lowered the LUMO levels and induced the preferential reduction of FSI (Fig. 6c). The free TTE molecules possessed higher LUMO levels, compared with those of the coordinated FSI and DMC (Fig. 6b), indicating that they were not easily reduced. However, the special molecular structure of TTE containing multiple F atoms induced the decomposition of a small amount of TTE, which provided more F atoms to attack Li and form an "LiF-rich" SEI layer, compared with that in the HCE, which was responsible for the enhanced cycling stability [56].

Following this orbital analysis, the reactivities of the electrolyte components were considered by supplying excess electrons to the simulation cell to correlate the LUMO levels and SEI layer composition in different electrolytes. The initial configurations were obtained by AIMD simulations with a neutral charge equal to zero (Fig. S8), after which electrons were sequentially added to the simulation cells (2 ps each) individually until there were four excess electrons. As shown in Fig. 6d, after the simulation, the coordinated DMC decomposed into OCH_3 and CH_3CO fragments in the LCE. The FSI coordinated with multiple Li^+ underwent defluorination reactions forming two F and N $(SO_2)_2$ in LHCE and HCE, followed by an F atom attack on Li to form LiF. The detailed reaction pathways are summarized in Fig. S8. In general, the results of the decomposition process correlated with those of the aforementioned LUMO level analysis.

X-ray photoelectron spectroscopy (XPS) was employed to characterize the chemical composition of the SEI layer formed in the three electrolytes. As shown in Fig. 7, C–H (C 1s, 285.02 eV); C–O (C 1s, 286.86 eV); and C═O (C 1s, 288.91 eV) were detected for the SEI layer formed in the LCE, which revealed a relatively high quantity of the

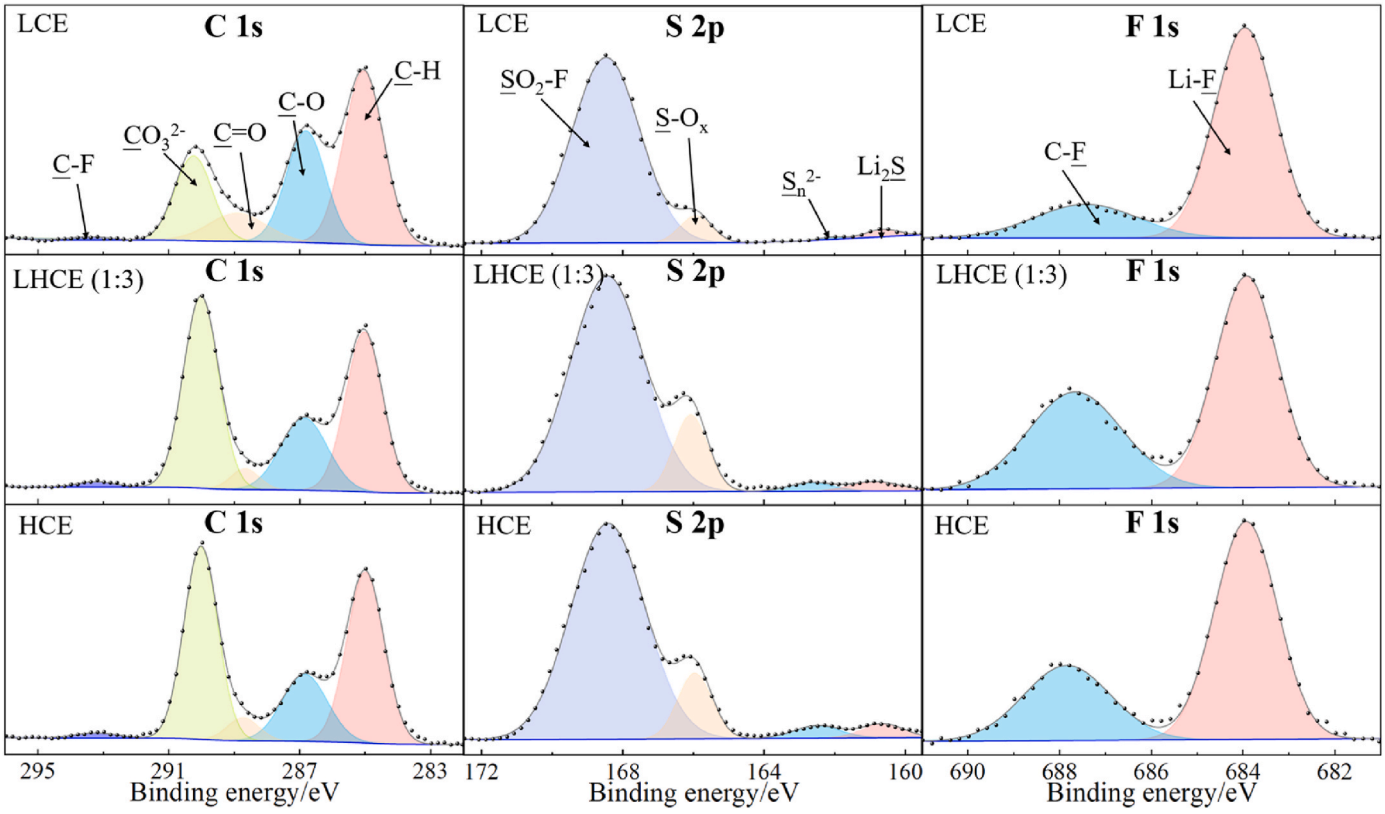

Fig. 7. XPS results of SEI components after the 10th cycle in different electrolytes.

decomposition of DMC. In contrast, the SEI layer with LHCE (1:3) and HCE demonstrated a reduced ratio of C–O and C═O, indicating that increasing the salt concentrations or adding TTE suppressed the decomposition of DMC. Furthermore, a high content of the CO_3^{2-} group in the SEI layer was detected for LHCE (1:3) and HCE, which stabilized the Li metal and was responsible for the enhanced plating/stripping cycling stability [58]. A relatively higher S-O_x was detected for LHCE (1:3) and HCE, verifying the result of the orbital analysis that the coordinated FSI preferentially decomposed in LHCE (1:3) and HCE. This tendency was confirmed by the larger peak area of F 1s in LHCE (1:3) and HCE, compared with that of LCE, which was mainly attributed to the defluorination reactions of the coordinated FSI . The unique microstructure of LHCE (1:3) was vital in determining the chemical composition of the SEI layer: (1) The local Li^+ solvation structure, similar to that of HCE, contributed to the predominant FSI decomposition. (2) The free TTE decomposition contributed to the formation of an "LiF-rich" SEI layer.

4. Conclusions

LHCE, with TTE as a diluent, was demonstrated to possess satisfactory physicochemical and electrochemical properties, compared with those of the LCE and HCE. The addition of the diluent enabled LHCE to exhibit a local ion solvation structure similar to that of HCE while enabling a unique microstructure of two well-defined domains, a Li(FSI)$_x$(DMC)$_y$ cluster and TTE-rich domain. The molecular mechanisms underlying the effect of the microstructural differences in LCE, LHCE, and HCE on dynamic and interfacial properties were explored with theoretical and experimental methods. The unique microstructure of LHCE induced the hopping diffusion of Li^+ through the FSI coordination layers inside the clusters, which was responsible for the high transference number and fast diffusion of Li^+. In addition, the FSI coordinated with multiple Li^+ exhibited the lowest LUMO levels and underwent defluorination reactions to contribute, with the TTE decomposition, to the formation of a stable and robust "LiF-rich" SEI layer. These systematic comparisons and fundamental insights clarified the causal relationship between the electrolyte microstructure and battery performance. In addition, it highlighted the importance of microstructural and dynamic heterogeneities of electrolytes in the rational design of advanced electrolytes for next-generation LMBs.

CRediT authorship contribution statement

Long Su: Conceptualization, Experiment, Simulation, Writing – original draft. **Fei Lu:** Investigation, Characterization, Discussion. **Xu Liu:** Cycling, EM and Impedance Experiment. **Chunting Wang:** XPS Experiment. **Yanan Gao:** Formal analysis, Discussion. **Stefano Passerini:** Supervision, Writing – review & editing. **Liqiang Zheng:** Supervision, Funding acquisition. **Gao Xinpei:** Conceptualization, Supervision, Funding acquisition, Writing – review & editing.

Declaration of competing interest

The authors declare that they have no known competing financial interests or personal relationships that could have appeared to influence the work reported in this paper.

Data availability

Data will be made available on request.

Acknowledgment

This work was supported by the National Natural Science Foundation of China (22102090, 21902092, 21960511), the Natural Science Foundation of Shandong Province (ZR2019ZD45). X.L. and S.P. acknowledge the basic funding of the Helmholtz Association.

References

[1] J.M. Tarascon, M. Armand, Issues and challenges facing rechargeable lithium batteries, Nature 414 (6861) (2001) 359–367.

[2] X.B. Cheng, R. Zhang, C.Z. Zhao, Q. Zhang, Toward safe lithium metal anode in rechargeable batteries: a review, Chem. Rev. 117 (15) (2017) 10403–10473.

[3] A. Mauger, M. Armand, C.M. Julien, K. Zaghib, Challenges and issues facing lithium metal for solid-state rechargeable batteries, J. Power Sources 353 (2017) 333–342.

[4] X. He, D. Bresser, S. Passerini, F. Baakes, U. Krewer, J. Lopez, C.T. Mallia, Y. Shao-Horn, I. Cekic-Laskovic, S. Wiemers-Meyer, F.A. Soto, V. Ponce, J.M. Seminario, P. B. Balbuena, H. Jia, W. Xu, Y.B. Xu, C.M. Wang, B. Horstmann, R. Amine, C.C. Su, J.Y. Shi, K. Amine, M. Winter, A. Latz, R. Kostecki, The passivity of lithium electrodes in liquid electrolytes for secondary batteries, Nat. Rev. Mater. 6 (11) (2021) 1036–1052.

[5] L. Kops, C. Leibing, L.H. Hess, A. Balducci, Mixtures of glyoxylic acetals and organic carbonates as electrolytes for lithium-ion batteries, J. Electrochem. Soc. 168 (1) (2021), 010513.

[6] G.T. Kim, S. Passerini, M. Carewska, G.B. Appetecchi, Ionic liquid-based electrolyte membranes for medium-high temperature lithium polymer batteries, Membranes 8 (3) (2018) 41.

[7] Y.C. Chen, Y.D. Jiang, S.S. Chi, H.J. Woo, K. Yu, J. Ma, J. Wang, C.Y. Wang, Y. H. Deng, Understanding the lithium dendrites growth in garnet-based solid-state lithium metal batteries, J. Power Sources 521 (2022), 230921.

[8] L.Y. Wei, N.P. Deng, J.G. Ju, J.B. Kang, X.X. Wang, L. Ding, W.M. Kang, B. W. Cheng, A review on nanofiber materials for lithium-metal batteries to suppress the dendritic lithium growth, Chem. Eng. J. 433 (2022), 134392.

[9] G. Yasin, M. Arif, T. Mehtab, X. Lu, D.L. Yu, N. Muhammad, M.T. Nazir, H.H. Song, Understanding and suppression strategies toward stable li metal anode for safe lithium batteries, Energy Storage Mater. 25 (2020) 644–678.

[10] M. Ue, K. Uosaki, Recent progress in liquid electrolytes for lithium metal batteries, Current Opinion in Electrochemistry 17 (2019) 106–113.

[11] S. Fang, L.F. Shen, A. Hoefling, Y. Wang, G. Kim, P.A. van Aken, X.G. Zhang, S. Passerini, A mismatch electrical conductivity skeleton enables dendrite-free and high stability lithium metal anode, Nano Energy 89 (2021), 106421.

[12] C. Leibing, A. Balducci, Glyoxylic-acetal-based electrolytes in combination with soft and hard carbon electrodes for lithium-ion batteries: an evaluation of room and high temperature performance, J. Electrochem. Soc. 168 (9) (2021), 090533.

[13] S. Brutti, E. Simonetti, M. De Francesco, A. Sarra, A. Paolone, O. Palumbo, S. Fantini, R. Lin, A. Falgayrat, H. Choi, M. Kuenzel, S. Passerini, G.B. Appetecchi, Ionic liquid electrolytes for high-voltage, lithium-ion batteries, J. Power Sources 479 (2020), 228791.

[14] J.G. Zhang, W. Xu, J. Xiao, X. Cao, J. Liu, Lithium metal anodes with nonaqueous electrolytes, Chem. Rev. 120 (24) (2020) 13312–13348.

[15] Q. Wang, H.C. Wang, J.Y. Wu, M.Y. Zhou, W. Liu, H.H. Zhou, Advanced electrolyte design for stable lithium metal anode: from liquid to solid, Nano Energy 80 (2021), 105516.

[16] S. Fang, L.F. Shen, S.P. Li, H. Dou, X.G. Zhang, Self-supported tin nanorod array/carbon textile as a lithium host that induces dendrite-free lithium plating with high rates and long cycle life, J. Mater. Chem. 8 (6) (2020) 3293–3299.

[17] Z. Yu, H. Wang, X. Kong, W. Huang, Y. Tsao, D.G. Mackanic, K. Wang, X. Wang, W. Huang, S. Choudhury, Y. Zheng, C.V. Amanchukwu, S.T. Hung, Y. Ma, E. G. Lomeli, J. Qin, Y. Cui, Z. Bao, Molecular design for electrolyte solvents enabling energy-dense and long-cycling lithium metal batteries, Nat. Energy 5 (7) (2020) 526–533.

[18] R. Xu, X.-Q. Zhang, X.-B. Cheng, H.-J. Peng, C.-Z. Zhao, C. Yan, J.-Q. Huang, Artificial soft-rigid protective layer for dendrite-free lithium metal anode, Adv. Funct. Mater. 28 (8) (2018), 1705838.

[19] S. Li, Z. Luo, L. Li, J. Hu, G. Zou, H. Hou, X. Ji, Recent progress on electrolyte additives for stable lithium metal anode, Energy Storage Mater. 32 (2020) 306–319.

[20] X.D. Ren, S.R. Chen, H. Lee, D.H. Mei, M.H. Engelhard, S.D. Burton, W.G. Zhao, J. M. Zheng, Q.Y. Li, M.S. Ding, M. Schroeder, J. Alvarado, K. Xu, Y.S. Meng, J. Liu, J. G. Zhang, W. Xu, Localized high-concentration sulfone electrolytes for high-efficiency lithium-metal batteries, Chem 4 (8) (2018) 1877–1892.

[21] J. Hu, Y. Ji, G. Zheng, W. Huang, Y. Lin, L. Yang, F. Pan, Influence of electrolyte structural evolution on battery applications: cationic aggregation from dilute to high concentration, Aggregate 3 (1) (2022) e153.

[22] S.M. Wang, J.Y. Qu, F. Wu, K. Yan, C.Z. Zhang, Cycling performance and kinetic mechanism analysis of a li metal anode in series-concentrated ether electrolytes, ACS Appl. Mater. Interfaces 12 (7) (2020) 8366–8375.

[23] F.L. Qiu, X. Li, H. Deng, D. Wang, X.W. Mu, P. He, H.S. Zhou, A concentrated ternary-salts electrolyte for high reversible Li metal battery with slight excess Li, Adv. Energy Mater. 9 (6) (2019), 1803372.

[24] Y. Yamada, J.H. Wang, S. Ko, E. Watanabe, A. Yamada, Advances and issues in developing salt-concentrated battery electrolytes, Nat. Energy 4 (5) (2019) 269–280.

[25] F.H. Ren, Z.D. Li, J.H. Chen, P. Huguet, Z. Peng, S. Deabate, Solvent-diluent interaction-mediated solvation structure of localized high-concentration electrolytes, ACS Appl. Mater. Interfaces (2022) 4211–4219.

[26] T. Li, Y. Li, Y.L. Sun, Z.F. Qian, R.H. Wang, New insights on the good compatibility of ether-based localized high-concentration electrolyte with lithium metal, ACS Materials Letters 3 (6) (2021) 838–844.

[27] X. Liu, A. Mariani, T. Diemant, M.E. Di Pietro, X. Dong, M. Kuenzel, A. Mele, S. Passerini, Difluorobenzene-based locally concentrated ionic liquid electrolyte enabling stable cycling of lithium metal batteries with nickel-rich cathode, Adv. Energy Mater. 12 (25) (2022), 2200862.

[28] X. Liu, M. Zarrabeitia, A. Mariani, X.P. Gao, H.M. Schutz, S. Fang, T. Bizien, G. A. Elia, S. Passerini, Enhanced Li^+ transport in ionic liquid-based electrolytes aided by fluorinated ethers for highly efficient lithium metal batteries with improved rate capability, Small Methods 5 (7) (2021), 2100168.

[29] X. Cao, H. Jia, W. Xu, J.-G. Zhang, Review—localized high-concentration electrolytes for lithium batteries, J. Electrochem. Soc. 168 (1) (2021), 010522.

[30] W. Dai, N. Dong, Y. Xia, S. Chen, H. Luo, Y. Liu, Z. Liu, Localized concentrated high-concentration electrolyte enhanced stability and safety for high voltage li-ion batteries, Electrochim. Acta 320 (2019), 134633.

[31] X. Cao, L. Zou, B.E. Matthews, L. Zhang, X. He, X. Ren, M.H. Engelhard, S. D. Burton, P.Z. El-Khoury, H.-S. Lim, C. Niu, H. Lee, C. Wang, B.W. Arey, C. Wang, J. Xiao, J. Liu, W. Xu, J.-G. Zhang, Optimization of fluorinated orthoformate based electrolytes for practical high-voltage lithium metal batteries, Energy Storage Mater. 34 (2021) 76–84.

[32] X. Liu, A. Mariani, M. Zarrabeitia, M.E. Di Pietro, X. Dong, G.A. Elia, A. Mele, S. Passerini, Effect of organic cations in locally concentrated ionic liquid electrolytes on the electrochemical performance of lithium metal batteries, Energy Storage Mater. 44 (2022) 370–378.

[33] M.J. Abraham, T. Murtola, R. Schulz, S. Páll, J.C. Smith, B. Hess, E. Lindahl, Gromacs: high performance molecular simulations through multi-level parallelism from laptops to supercomputers, Software 1–2 (2015) 19–25.

[34] L. Su, X.P. Gao, A. Mariani, X. Liu, S. Passerini, Y.A. Gao, L.Q. Zheng, Molecular insight into microstructural and dynamical heterogeneities in magnesium ionic liquid electrolytes, J. Phys. Chem. Lett. 13 (1) (2022) 105–111.

[35] A. Mariani, R. Caminiti, F. Ramondo, G. Salvitti, F. Mocci, L. Gontrani, Inhomogeneity in ethylammonium nitrate-acetonitrile binary mixtures: the highest "low q excess" reported to date, J. Phys. Chem. Lett. 8 (15) (2017) 3512–3522.

[36] K. Shimizu, D. Almantariotis, M.F.C. Gomes, A.A.H. Padua, J.N.C. Lopes, Molecular force field for ionic liquids v: hydroxyethylimidazolium, dimethoxy-2-methylimidazolium, and fluoroalkylimidazolium cations and bis(fluorosulfonyl) amide, perfluoroalkanesulfonylamide, and fluoroalkylfluorophosphate anions, J. Phys. Chem. B 114 (10) (2010) 3592–3600.

[37] G. Kumar, T.R. Kartha, B.S. Mallik, Novelty of lithium salt solution in sulfone and dimethyl carbonate-based electrolytes for lithium-ion batteries: a classical molecular dynamics simulation study of optimal ion diffusion, J. Phys. Chem. C 122 (46) (2018) 26315–26325.

[38] S. Saito, H. Watanabe, K. Ueno, T. Mandai, S. Seki, S. Tsuzuki, Y. Kameda, K. Dokko, M. Watanabe, Y. Umebayashi, Li(+) local structure in hydrofluoroether diluted li-glyme solvate ionic liquid, J. Phys. Chem. B 120 (13) (2016) 3378–3387.

[39] L. Martinez, R. Andrade, E.G. Birgin, J.M. Martinez, Packmol: a package for building initial configurations for molecular dynamics simulations, J. Comput. Chem. 30 (13) (2009) 2157–2164.

[40] B. Hess, C. Kutzner, D. van der Spoel, E. Lindahl, Gromacs 4: algorithms for highly efficient, load-balanced, and scalable molecular simulation, J. Chem. Theor. Comput. 4 (3) (2008) 435–447.

[41] H.J.C. Berendsen, J.P.M. Postma, W.F. Vangunsteren, A. Dinola, J.R. Haak, Molecular-dynamics with coupling to an external bath, J. Chem. Phys. 81 (8) (1984) 3684–3690.

[42] G. Bussi, D. Donadio, M. Parrinello, Canonical sampling through velocity rescaling, J. Chem. Phys. 126 (1) (2007), 014101.

[43] D.M. York, T.A. Darden, L.G. Pedersen, The effect of long-range electrostatic interactions in simulations of macromolecular crystals - a comparison of the ewald and truncated list methods, J. Chem. Phys. 99 (10) (1993) 8345–8348.

[44] B. Hess, H. Bekker, H.J.C. Berendsen, J.G.E.M. Fraaije, Lincs: a linear constraint solver for molecular simulations, J. Comput. Chem. 18 (12) (1997) 1463–1472.

[45] J. VandeVondele, M. Krack, F. Mohamed, M. Parrinello, T. Chassaing, J. Hutter, Quickstep: fast and accurate density functional calculations using a mixed Gaussian and plane waves approach, Comput. Phys. Commun. 167 (2) (2005) 103–128.

[46] J.P. Perdew, K. Burke, M. Ernzerhof, Generalized gradient approximation made simple, Phys. Rev. Lett. 77 (18) (1996) 3865–3868.

[47] T. Lu, F.W. Chen, Multiwfn: a multifunctional wavefunction analyzer, J. Comput. Chem. 33 (5) (2012) 580–592.

[48] T. Li, Y. Li, Y. Sun, Z. Qian, R. Wang, New insights on the good compatibility of ether-based localized high-concentration electrolyte with lithium metal, ACS Materials Letters 3 (6) (2021) 838–844.

[49] N.T. Hahn, J. Self, K.S. Han, V. Murugesan, K.T. Mueller, K.A. Persson, K. R. Zavadil, Quantifying species populations in multivalent borohydride electrolytes, J. Phys. Chem. B 125 (14) (2021) 3644–3652.

[50] X. Gao, F. Wu, A. Mariani, S. Passerini, Concentrated ionic-liquid-based electrolytes for high-voltage lithium batteries with improved performance at room temperature, ChemSusChem 12 (18) (2019) 4185–4193.

[51] L. Yu, S. Chen, H. Lee, L. Zhang, M.H. Engelhard, Q. Li, S. Jiao, J. Liu, W. Xu, J.-G. Zhang, A localized high-concentration electrolyte with optimized solvents and lithium difluoro(oxalate)borate additive for stable lithium metal batteries, ACS Energy Lett. 3 (9) (2018) 2059–2067.

[52] L. Qin, N. Xiao, J. Zheng, Y. Lei, D. Zhai, Y. Wu, Localized high-concentration electrolytes boost potassium storage in high-loading graphite, Adv. Energy Mater. 9 (44) (2019), 1902618.
[53] L.L. Jiang, C. Yan, Y.X. Yao, W. Cai, J.Q. Huang, Q. Zhang, Inhibiting solvent co-intercalation in a graphite anode by a localized high-concentration electrolyte in fast-charging batteries, Angew. Chem. Int. Ed. 60 (7) (2021) 3402–3406.
[54] S. Chen, J. Zheng, D. Mei, K.S. Han, M.H. Engelhard, W. Zhao, W. Xu, J. Liu, J. G. Zhang, High-voltage lithium-metal batteries enabled by localized high-concentration electrolytes, Adv. Mater. 30 (21) (2018), e1706102.
[55] C. Wan, M.Y. Hu, O. Borodin, J. Qian, Z. Qin, J.-G. Zhang, J.Z. Hu, Natural abundance 17o, 6li nmr and molecular modeling studies of the solvation structures of lithium bis(fluorosulfonyl)imide/1,2-dimethoxyethane liquid electrolytes,
J. Power Sources 307 (2016) 231–243.
[56] Y. Wang, R. Jiang, Y. Liu, H. Zheng, W. Fang, X. Liang, Y. Sun, R. Zhou, H. Xiang, Enhanced sodium metal/electrolyte interface by a localized high-concentration electrolyte for sodium metal batteries: first-principles calculations and experimental studies, ACS Appl. Energy Mater. 4 (7) (2021) 7376–7384.
[57] Z. Yu, N.P. Balsara, O. Borodin, A.A. Gewirth, N.T. Hahn, E.J. Maginn, K. A. Persson, V. Srinivasan, M.F. Toney, K. Xu, K.R. Zavadil, L.A. Curtiss, L. Cheng, Beyond local solvation structure: nanometric aggregates in battery electrolytes and their effect on electrolyte properties, ACS Energy Lett. (2021) 461–470.
[58] M. Asadi, B. Sayahpour, P. Abbasi, A.T. Ngo, K. Karis, J.R. Jokisaari, C. Liu, B. Narayanan, M. Gerard, P. Yasaei, X. Hu, A. Mukherjee, K.C. Lau, R.S. Assary, F. Khalili-Araghi, R.F. Klie, L.A. Curtiss, A. Salehi-Khojin, A lithium-oxygen battery with a long cycle life in an air-like atmosphere, Nature 555 (7697) (2018) 502–506.